3D-PTV flow measurements of Newtonian and non-Newtonian fluid blending in a batch reactor in the transitional regime

Romano, M. G.; Alberini, F.; Liu, L.; Simmons, M. J.H.; Stitt, E. H.

[Link to publication on Research at Birmingham portal](#)

3D-PTV flow measurements of Newtonian and non-Newtonian fluid blending in a batch reactor in the transitional regime

M. G. Romano[1,2], F. Alberini[2], L. Liu[1], M. J. H. Simmons[2], E. H. Stitt[1]

[1] Johnson Matthey Technology Centre, Chilton Site, TS23 1LH, UK

[2] School of Chemical Engineering, University of Birmingham, B15 2TT, UK

Corresponding author email: manuele.romano@matthey.com

Abstract: Lagrangian trajectories obtained through 3D Particle Tracking Velocimetry (3D-PTV) measurements have been used to visualize the flow field of Newtonian and non-Newtonian fluids in a flat-bottomed vessel. The vessel, of diameter $T = 180$ mm, was equipped with a 6-blade Rushton turbine of diameter $D = T/3$ and four baffles of width $b = T/10$. The experiments were carried out in the transitional flow regime ($73 \leq Re \leq 1,257$). The velocities and Lagrangian accelerations in the flows have been calculated from the time-resolved tracer coordinates. Non-Newtonian fluids exhibited a smaller impeller flow number compared to Newtonian fluids. The distributions of shear rate have been obtained via interpolation of the Lagrangian velocity data in a 3D Eulerian grid. In the impeller region, the mean shear rate was, to a first approximation, proportional to the impeller rotational speed, although a more detailed analysis revealed influences of both rheology and Reynolds number. The mean Lagrangian acceleration scaled with the mean shear rate raised to the power of 1.8.

Keywords: PTV, mixing, stirred tanks, trajectories, Lagrangian, non-Newtonian, transitional.

1. Introduction

Mixing of liquids in mechanically agitated vessels is one of the most common and yet complex unit operations in the process industry. Such vessels have a key role in the production of many types of formulated products which possess both simple and complex rheology, such as foods, catalyst slurries and ink, paints, cosmetics and pharmaceuticals (Hemrajani and Tatterson, 2004). Control of the mixing performance, or the degree of segregation (Kukukova et al., 2011) is critical for successful product manufacture, ensuring batch to batch consistency and product quality. This is strongly influenced by both process and product parameters, primarily the mixer geometry and fluid rheology (Story et al., 2018).

Parameters which need to be specified for the mixer geometry include impeller type, such as the benchmark Rushton disc turbine radial impeller, shape of vessel bottom and whether baffles are installed. Specific power consumption, mixing time, pumping capacity, shear rate distribution and flow patterns are the most used criteria for impeller selection (Ameur and Bouzit, 2012). Baffles are solid surfaces that can be arranged orthogonally to the tangential flow to limit solid-body rotation of the fluid and enhance axial recirculation. Other geometrical parameters which impact the mixing performance include the impeller-to-tank diameter ratio, submergence, eccentricity and tilting angle from the vertical axis.

The rheology of complex high value added liquid products such as cosmetics, paints and foods are rarely Newtonian (Dickey, 2015), with the apparent viscosity, μ_e, being a function of the local shear rate, $\dot{\gamma}$, and possibly time, if the fluid is time-dependent. A myriad of constitutive laws have been postulated to describe this function, two of the most common being Ostwald-de Waele (power law), for shear-thickening and shear thinning fluids and Bingham, for fluids which exhibit a yield stress (Barnes et al., 1989). Such fluids behave very differently from a Newtonian fluid in a stirred vessel because the wide range of shear rates experienced cause corresponding large changes in local apparent viscosity. Away from the

impeller and near walls and baffles, shear forces are low, and the viscosity can be very high. These zones of the tank control the blending time (Grenville, 1992) and may remain unmixed because of inadequate fluid motion (Dickey, 2015). Yield stress liquids tend to form caverns of moving fluid around the impeller, while the fluid outside remains static. Viscous shear thinning liquids may form pseudo-caverns, outside of which the velocity is extremely low.

The flow regime in stirred vessels may be determined via the modified impeller Reynolds number, $Re = \frac{\rho N D^2}{\mu}$, where ρ is the fluid density, D is the impeller diameter and N is the impeller frequency. Its relationship to the power drawn, P, is a long-established function of the power number, $Po = \frac{P}{\rho N^3 D^5}$. For a non-Newtonian fluid, μ is replaced by μ_e. Po is inversely proportional to Re in the laminar regime, i.e. $Po = K_P Re^{-1}$, and constant in the turbulent regime, i.e. $Po = Po_T$. For a given geometry, the power number data of any Newtonian fluid will lie on the same curve. These plots are commonly used to select the impeller for a certain application and to predict the power consumption. The power curves of common geometries and the extension of flow regimes have been measured by many authors. For instance, in the case of the Rushton turbine, $K_P \approx 68$ for $Re \leq 10$ (Cabaret et al., 2008) and $Po_T \approx 5$ (Distelhoff et al., 1995). In the literature, $Re \geq 2 \times 10^4$ is commonly considered enough to sustain a fully turbulent flow in the vessel (Machado et al., 2013). However, since most of the energy provided by the impeller is dissipated in the impeller discharge stream (Zhou and Kresta, 1996), it is not guaranteed that the whole flow is fully turbulent. Additional requirements are the scaling of the mean velocity and of energy dissipation. Machado et al. (2013) applied Laser Doppler Anemometry (LDA) to measure the fluid velocity in vessels of different scales and configurations. They found that only a portion of the tank was fully turbulent at $Re = 2 \times 10^4$. Interestingly, Newtonian fluids of different viscosity mixed at

identical values of Reynolds number could present different flow regimes at the same location in the tank.

The situation becomes even more complex with non-Newtonian fluids. The Metzner-Otto model (Metzner and Otto, 1957) has become the most widely used method for estimating the power requirements of non-Newtonian fluids (Márquez-Baños et al., 2019) and is commonly recommended as a standard procedure in mixing text books (Doraiswamy et al., 1994). It assumes that, in laminar flows, the fluid motion in the impeller region is characterized by an effective shear rate, which is proportional to the impeller speed:

$$\dot{\gamma}_e = k_s N. \tag{1}$$

The apparent (also indicated as effective) viscosity, μ_e, is calculated at that value of shear rate, according to the fluid rheological model. The value of k_s is fitted so that the power number curve of any non-Newtonian fluid matches the curve for Newtonian fluids. The Metzner-Otto equation (1) was originally developed for flat-blade turbines operated at $2 \leq Re \leq 270$, and the authors reported a value of $k_s = 13$, which appeared to be independent of the fluid rheology, the impeller-to-tank diameter ratio, D/T, and the presence of baffles. However, the authors did not exclude an effect of the flow index, which was not varied widely in their work. They also suggested that, with close-clearance impellers such as ribbons or anchors, the effective shear rate could become dependent on D/T. Subsequent works have tried to determine the dependence of k_s on the fluid rheology and geometrical ratios, with significant discrepancies reported (e.g. Calderbank and Moo-Young, 1961; Nagata et al., 1971; Beckner and Smith, 1996).

Bertrand et al. (1996) extended the Metzner-Otto concept to yield stress fluids agitated with anchor impellers. They found that k_s was independent of Bi for $Bi \leq 7500$, where, $Bi = \frac{\tau_0}{KN^n}$, is the Bingham number, τ_0 is the yield stress K is the consistency index and n is the power law exponent (this definition assumes $\dot{\gamma}_e = N$). However, Anne-Archard et al. (2006)

simulated yield stress fluid flows induced by helical and anchor agitators and observed that k_s changed with Bi in the range $60 \leq Bi \leq 12,000$.

In the original Metzner-Otto approach, the shape and size of the impeller region were not specified and thus k_s was intended as a global parameter that could be determined through power measurements. More generally, the ratio between a volume-averaged shear rate and the impeller speed, i.e. $k_s^*(\Omega) = \langle \dot{\gamma} \rangle_\Omega / N$, is a function of the volumetric domain, Ω, and can be evaluated from local velocity data obtained either by experiment or by simulation using Computational Fluid Dynamics (CFD). For example, Jahangiri et al. (2001) investigated the flow of four viscoelastic polyacrylamide solutions within a vessel stirred with a Rushton turbine under transitional conditions and evaluated, by means of LDA, the shear rate from the velocity data at different radial positions. At the impeller tip, k_s^* varied between 10.22 and 10.50. Ramírez-Muñoz et al. (2017) used CFD to simulate the flow induced by a Rushton turbine and divided the impeller region into many control volumes. In each volume, k_s^* was calculated from the volume-averaged shear rate and a value of $k_s^* = 11.8$ was obtained in the volume swept by the impeller blades. This is very close to the value of $k_s = 11.1$ fitted directly from power measurements and to the typical value of $k_s = 11.5$ reported in the literature. Márquez-Baños et al. (2019) carried out a similar analysis for a pitched-blade turbine, though in that case, a larger volume than that swept by the impeller blades had to be considered to match the volume-based k_s^* with the power-based k_s.

As the Reynolds number increases, the characteristic shear rate diverges from the Metzner-Otto model (1) and becomes proportional to $N^{3/2}$ (Sánchez Pérez et al., 2006) due to the turbulence contribution to shear generation. Nonetheless, due to its simplicity, the Metzner-Otto model is commonly applied outside of laminar flow conditions (Böhme and Stenger, 1988). Kelly and Gigas (2003) simulated the flow of Newtonian and power-law liquids ($0.4 \leq n \leq 0.8$) near axial flow impellers operating in the transitional regime. They found that the

shear rate around the impeller surface could be approximated as a linear function of the impeller frequency, but upon closer inspection it also depended on the flow index. This was because the impeller discharge angle changed dramatically with both Re and n. Using Newtonian data from Kelly and Gigas (2003), Sánchez Pérez et al. (2006) observed that a power-law fitting of the impeller shear with $N^{1.4}$ provided a higher coefficient of determination than the linear fitting ($R^2 = 0.99$ instead of $R^2 = 0.95$). However, given the small number of data points, the 4% increase in R^2 is not enough to demonstrate a better fitting. More likely, this was just an effect of the additional degree of freedom introduced by the power law model.

The flow number, $Fl = \frac{Q}{ND^3}$, normalizes the flow rate of fluid circulated by the impeller, Q. In the case of a Rushton turbine, which pumps the fluid radially, Q can be obtained from velocity data as the flux across a control surface parallel to the impeller blade height (Dyster et al., 1993):

$$Q(s) = 2\pi \left(\frac{D}{2} + s\right) \int_{c-w/2}^{c+w/2} \overline{U_r} \, dy. \tag{2}$$

In (2), $\overline{U_r}$ is the azimuthally averaged radial component of the velocity at a radial coordinate $r = D/2 + s$, where s is an arbitrary distance from the impeller tip, c is the vertical coordinate of the impeller plane and w is the vertical size of the impeller blade. Norwood and Metzner (1960) measured the flow rates of Newtonian fluids with Rushton turbines. In the range of Re between 36 and 1.7×10^4, the flow rates were

$$Q \propto ND^2 w \left(D^{0.4} \frac{\rho}{\mu}\right)^{0.5} (1 - q^2)^{0.5}. \tag{3}$$

The term q, representing the difference between the impeller velocity and the fluid velocity at the blade tip, was found to be negligible. In the laminar and transitional regimes, the flow number depends on the Reynolds number, then it becomes constant under turbulent conditions. Dyster et al. (1993) measured Fl of the Rushton turbine in a range of Re between 5 and $5 \cdot 10^4$

with Newtonian fluids, based on the mean velocity profiles. They found that Fl was proportional to $Re^{0.5}$ till $Re \leq 500$, and it approached a constant value of ~0.78 for $Re > 500$. The profiles of the root mean square (rms) values of the radial velocity, normalized by the impeller tip speed, were also independent of Re for $Re > 500$. Koutsakos and Nienow (1990) conducted a similar analysis with shear thinning liquids ($0.37 \leq n \leq 0.58$). The value of flow number of shear thinning fluids was always smaller than that for Newtonian fluids at the same Reynolds number. In particular, Fl was proportional to Re for $Re \leq 60$ and to $Re^{0.2}$ for $Re > 60$, till eventually it reached the constant value of ~0.78. Venneker et al. (2010) measured the velocity profiles of ten liquids ($0.56 \leq n \leq 1$) agitated with a Rushton turbine. The Reynolds number of the experiments varied from the transitional ($Re \sim 10^3$) to the turbulent regime ($Re \sim 10^5$). The flow index was found to have a different impact on the various velocity components (both mean and rms). The shear thinning rheology had a widening effect on the discharge profiles of the radial and tangential velocities, resulting in lower flow numbers compared to the Newtonian liquids. However, the differences were not as pronounced as in Koutsakos and Nienow (1990).

In industry, mixing operations in stirred vessels are frequently carried out under transitional flow conditions. However, most experimental and numerical studies reported in the literature focus on fully laminar or fully turbulent flows (Mendoza et al., 2018). Therefore, the transitional regime is still not well characterised (Machado et al., 2013), particularly when non-Newtonian rheology is involved. Furthermore, most experimental studies in agitated vessels have been carried out by means of Eulerian techniques, including PIV, LDA and Planar Laser Induced Fluorescence (PLIF). Lagrangian investigations of fluid mixing in stirred tanks have been rather limited. Some examples include the works by Rammohan et al. (2001, 2003) with Computer Automated Radioactive Particle Tracking (CARPT) and Chiti et al. (2011) using Positron Emission Particle Tracking (PEPT). Alberini et al. (2017) have applied PTV to

transitional flows of non-Newtonian fluids in agitated vessels, but their analysis was limited to a comparison of the interpolated Eulerian velocity against PIV data. This paper presents a novel investigation of the agitation of Newtonian and non-Newtonian fluids in a lab-scale vessel equipped with a Rushton turbine under transitional flow conditions using 3D-PTV. The effects of the fluid rheology on the flow dynamics have been assessed in terms of mean flow patterns, impeller flow numbers and distributions of shear rate and Lagrangian acceleration. A study of the volume-averaged shear rate in the impeller region has been carried out to test the validity of Metzner-Otto's assumption in the low and mid transitional flow regime. To the best of the authors' knowledge, this is the first time that PTV has been applied to fluid mixing in agitated vessels in a wide range of experimental conditions.

2. Materials and methods

2.1. Flow systems and experimental conditions

The flows investigated in this work were obtained by agitating different fluids in a transparent flat-bottomed cylindrical vessel of diameter $T = 180$ mm and height $H = T$. The tank was equipped with four baffles, of width $b = T/10$, and a 6-blade Rushton disc turbine, of diameter $D = T/3$ and placed at a clearance $c = T/3$ from the bottom. The impeller blades had width $D/4$, height $D/5$ and thickness of 2 mm. The geometry of the flow system is pictured in Fig. 1. The main vessel was immersed a larger transparent square tank, filled with the same liquid, in order to minimize refractive distortion at the curved wall.

The six working fluids used were aqueous solutions of glycerol (75% and 80% wt. concentration), carboxymethylcellulose (CMC, 0.5% and 1.0% wt.) and polyacrylic acid (Carbopol 940, 0.1% wt. at pH 5.5 and 0.15% wt. at pH 5.0) at room temperature. The materials were purchased from Sigma-Aldrich, US. The two glycerol solutions exhibited Newtonian

rheology, as expected. The power-law model (4) and the Herschel-Bulkley model (5) were used to describe the rheology of the CMC and Carbopol solutions, respectively.

$$\mu_{PL} = K\,\dot{\gamma}^{n-1};$$ (4)

$$\mu_{HB} = K\,\dot{\gamma}^{n-1} + \tau_0\dot{\gamma}^{-1}.$$ (5)

Note that for $n = 1$ and $\tau_0 = 0$ the two models reduce to a Newtonian fluid with constant viscosity. The rheological parameters of the fluids (Table 1) were measured with a rheometer (Discovery HR-1 by TA Instruments) equipped with a 40 mm flat plate geometry. K and n have been obtained through fitting of the flow sweep curves, while τ_0 has been determined at the crossover point of the loss and storage moduli, through amplitude sweep measurements at a frequency of 10 Hz.
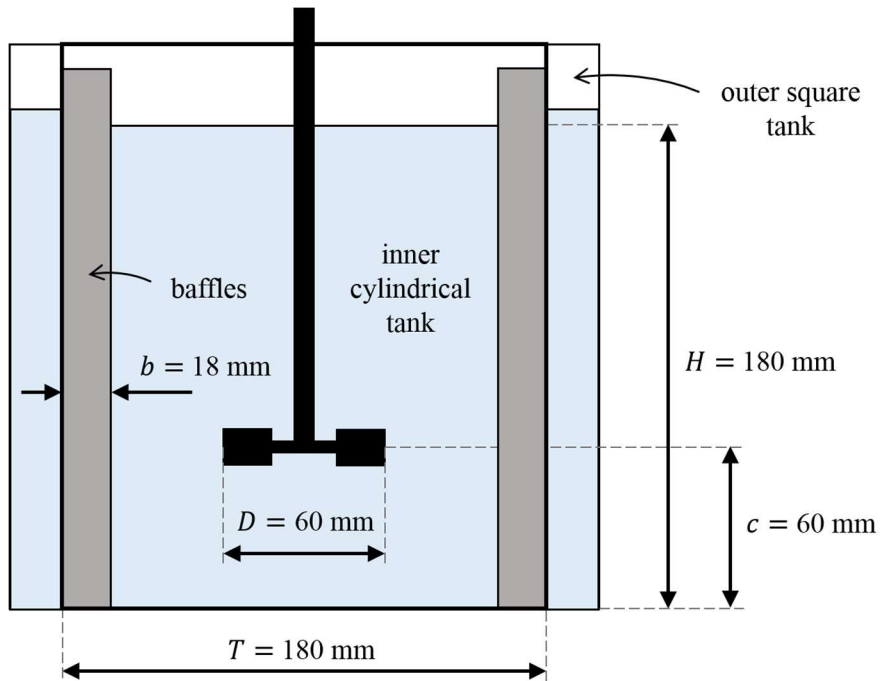

Figure 1: Schematic of the agitated vessel.

Table 1: Rheological parameters of the working fluids.

Label	Composition (in water)	$K\,[Pa\,s^n]$	$n\,[-]$	$\tau_0\,[Pa]$

NW1	Glycerol 75% wt.	0.046	1	0
NW2	Glycerol 80% wt.	0.17	1	0
PL1	CMC 0.5% wt.	0.20	0.7	0
PL2	CMC 1.0% wt.	0.70	0.7	0
HB1	Carbopol 0.10% wt. (pH 5.5)	1.1	0.5	4.2
HB2	Carbopol 0.15% wt. (pH 5.0)	4.4	0.5	43

Each liquid was mixed at various impeller speeds to obtain observations at different Reynolds numbers (Table 2). Although the flow regime was transitional, the Metzner-Otto model ($k_s = 11.5$) was used to estimate the apparent viscosity and Reynolds number of non-Newtonian fluids.

Table 2: Experimental conditions.

Experiment	Fluid	Impeller speed (rpm)	Camera frame rate (s^{-1})	μ_e (Pa s)	Re (-)
NW1a		400	250		629
NW1b	NW1	600	500	$4.60 \cdot 10^{-2}$	943
NW1c		800	500		1,257
NW2a	NW2	200	125	$1.70 \cdot 10^{-1}$	86

NW2b		600	250		258
PL1a		100	60	$8.25\ 10^{-2}$	73
PL1b	PL1	200	125	$6.70\ 10^{-2}$	179
PL1c		400	250	$5.44\ 10^{-2}$	441
PL1d		800	500	$4.42\ 10^{-2}$	1,086
PL2a	PL2	400	125	$1.90\ 10^{-1}$	126
PL2b		800	250	$1.55\ 10^{-1}$	310
HB1a		400	125	$1.80\ 10^{-1}$	133
HB1b	HB1	600	250	$1.39\ 10^{-1}$	259
HB1c		800	250	$1.16\ 10^{-1}$	413
HB1d		1,000	500	$1.01\ 10^{-1}$	592
HB2a	HB2	1,200	500	$4.77\ 10^{-1}$	151
HB2b		1,500	1,000	$4.09\ 10^{-1}$	220

2.2. 3D-PTV measurements

3D-PTV is based on individual tracking of many flow tracers in 3D space and time. The principles of the technique are thoroughly discussed in Maas et al. (1993) and Malik et al. (1993). In summary, a 3D-PTV experiment consists of the following steps:

1) Acquisition of a stereoscopic sequence of synchronous images.

2) Detection of the tracers and determination their image coordinates.

3) Establishment of the stereoscopic correspondences and determination of the tracer 3D coordinates.

4) Establishment of the temporal links across subsequent frames.

5) Determination of the velocity.

PTV has been used successfully in a variety of practical applications, using small observation volumes (e.g. Monica et al., 2009; Kinzel et al., 2011; Gülan et al., 2012; Krug et al., 2012; Gallo et al. 2014; Krug et al., 2014; Oliveira et al., 2015; Aguirre-Pablo et al., 2019) and for the study of turbulence statistics at small scales (e.g. Lüthi et al., 2005; Holzner et al., 2008; Liberzon et al., 2012). Romano et al. (2021) assessed the capability of 3D-PTV to measure the flow dynamics in lab scale stirred vessels, under proper choice of the operational variables.

2.2.1. Tracer particles

Polyethylene microspheres (Cospheric, US) have been used as tracer particles. Their size was $750 - 820$ μm. The tracers utilized with the CMC and Carbopol solutions had a density of 1.0×10^3 kg m^{-3}. For the glycerol solutions, the tracer density was 1.1×10^3 kg m^{-3}. Buoyancy effects were negligible. The Stokes number is the ratio between the relaxation time of a tracer, t_P, and a characteristic time scale of the flow, t_F. Small values indicate that the tracer can rapidly and faithfully respond to the variations of the flow, down to length scales comparable to the tracer size. The Stokes number is therefore widely used as a measure of the fidelity of a particle tracking experiment. In the Stokesian regime, the particle time is conventionally calculated applying the Stokes drag law to a particle moving in the fluid:

$$St_L = \frac{\dfrac{\rho_P d_P{}^2}{18\,\mu}}{t_F},$$

(6)

where ρ_P is the particle density, d_P is the particle size and μ is the fluid viscosity. In this paper, the characteristic flow macroscopic time scale was expressed as $t_F = 1/6N$, that is the time between two consecutive impeller blade passages. For a conservative estimate, the viscosity of the non-Newtonian fluids was calculated at a shear rate equal to $10\,\dot{\gamma}_e = 115\,N$. The Stokes law underestimates the drag force on the particle when the flow is non-Stokesian and overpredicts the relaxation time. Israel and Rosner (1982) generalized the Stokes number in non-Stokesian flow regimes introducing a correction factor $\psi < 1$:

$$St = \psi St_L. \tag{7}$$

Wessel and Righi (1988) provided an analytical correlation for ψ for particle Reynolds number $Re_p = \rho U_{rel} d_p / \mu < 10^3$:

$$\psi = \frac{3\left(\sqrt{c}Re_p^{1/3} - \text{atan}\left(\sqrt{c}Re_p^{1/3}\right)\right)}{c^{3/2}Re_p}, \tag{8}$$

with $c = 0.158$. The relative velocity was estimated as $U_{rel} \sim 1\%\ U_{tip}$. The corrected Stokes numbers ranged from 2.4×10^{-3} (experiment PL1a, $\psi = 0.998$) to 1.1×10^{-1} (experiment PL2b, $\psi = 0.92$). These estimates are highly conservative, as it will be shown that the maximum shear rate observed in the impeller region was $<40\,N$ (Figure 7a), thus fluid viscosity was higher. Also, the flow would lose memory of the blade passage away from the impeller, hence the flow time scales were larger. Romano et al. (2021) showed that at $Re = 12,000$ the time scales obtained from the Lagrangian velocity autocorrelation were in the order of the impeller period, i.e. $1/N$. When $St < \sim 10^{-1}$, the errors in flow tracing are negligible (McKeon et al., 2007). Chiti et al. (2011) validated their PEPT measurements of a turbulent stirred tank flow against the literature, despite $St \sim 0.6$. Appreciable errors in the velocities were only present very close to the impeller tip. Given that the turbulence scales were not investigated in this paper, it was concluded that the tracers could adequately resolve the mean flow features

down to a scale of ~820 μm. The effects of Magnus force, Basset force and Saffman force were negligible.

The tracer concentration was roughly 114 L^{-1}, which corresponded to a blur image density of 0.002 px^{-2}. With a particle image size between 3 and 4 px, the ratio of indistinguishably overlapping particles was between 0.7% and 1.2% (Cierpka et al., 2013).

2.2.2. Image acquisition and processing

The raw images of the flows were acquired through a high-speed camera (Fastcam SA4, Photron Ltd., JP) equipped with a macro lens (Sigma 24-70 mm f2.8 EX DG Macro, Nikon, JP). A system of mirrors (LINOS adjust.X, Qioptiq, UK) allowed the vessel to be imaged from two viewing orientations in a single image. LED lights (Marathon multiLED LT, GSVitec GmbH, DE) were used for the illumination. The raw images were encoded in a 8-bit greyscale (levels from 0 and 255) at 1024×1024 px^2 resolution. Each experiment consisted of 5,400 frames. The acquisition rate (Table 2) was selected depending on the impeller speed and an estimation of the experimental error, following the guidelines discussed in Romano et al. (2021). The distance travelled by the tracers between consecutive time steps was in the order of $1 - 10$ mm, depending on their velocity. The exposure time was 1/2000 s for the two CMC solutions and 1/3600 s for all other fluids, so that tracers appeared spherical in the images.

The images were processed as described in Romano et al. (2021). The output of this step consisted in a list containing the image coordinates of the detected tracers, in each half-image and each time step.

2.2.3. Image calibration

The image calibration was conducted using a reference geometry with 147 control dots spanning a volume of $60 \times 200 \times 55$ mm^3 in x (width), y (height) and z (depth). The calibration routine was conducted as described in Romano et al. (2021). In summary, the coordinate

transformation matrix of each viewing orientation was determined based on 147 correspondences between the image coordinates and the known world coordinates of the control dots. By knowing the two transformation matrices, any point in 3D space could be determined from the paired image coordinates through the method of epipolar lines. The mathematical aspects of stereoscopic imaging, calibration and 3D reconstruction can be found in Maas et al. (1993).

In PTV experiments, the error in the reconstructed tracer coordinates is determined by the quality of the image calibration. This is influenced by the properties of the multi-media optical path, the fluid opaqueness in particular. The glycerol and Carbopol solutions were highly transparent, and the reference dots were reconstructed with an average error of ~60 μm. In the case of the CMC solutions, which were slightly opaque, the average reconstruction error was ~180 μm. These errors were reduced before the computation of velocity and acceleration by means of a Savitzky-Golay filter.

2.2.4. Stereo-matching, 3D tracking, velocity and acceleration determination

The stereoscopic correspondences were established with the method of epipolar lines. To limit the stereoscopic ambiguities and allow to work with only two viewing orientations, the algorithm developed by Willneff (2003) was used. Given the previous tracer positions, the correct link among many candidates at the following time step was determined by minimizing the change in Lagrangian acceleration. Trajectories longer than 21 time steps were kept to minimize the chance of wrong stereo and temporal links. In addition, only the data in the front half of the tank ($z < 0$) were used. This was because the coordinates at the back ($z < 0$) were determined with a larger uncertainty, due to perspective size reduction of the tracers and attenuation of the scattered light through the longer optical path.

The velocity components along the individual trajectories were obtained by finite differentiation of the coordinates. To avoid amplification of the experimental error, a second

order, 11-point Savitzky-Golay filter (Savitzky and Golay, 1964) was applied. This means that the local tracers dynamics was described as uniformly accelerated. This assumption has been confirmed by Malik et al. (1993) and Romano et al. (2021) and is consistent with the tracking criterion of minimizing the change in Lagrangian acceleration. The velocity components along the trajectories were calculated with a centred differences scheme from the corresponding coordinates (eq. 9), and then filtered themselves. In the same way, the Lagrangian acceleration components were obtained through differentiation of the velocities (eq. 10) and then filtered.

$$u_j = \frac{x_{j+1} - x_{j-1}}{t_{j+1} - t_{j-1}}. \tag{9}$$

$$a_j = \frac{u_{j+1} - u_{j-1}}{t_{j+1} - t_{j-1}}. \tag{10}$$

In the equations above, the subscript j indicates the time step. The Lagrangian acceleration is a measure of the force acting on an infinitesimal element of fluid which moves with the local and instantaneous flow. It is responsible for stretching, contraction and curvature of the fluid element. The statistics of Lagrangian acceleration are of great importance in turbulence research, as they are related to the intermittent bursts of vorticity and strain that characterize turbulent flows (Zeff et al., 2003). Large values of acceleration and energy dissipation are strongly correlated (Reynolds et al., 2005). However, to the authors' knowledge, Lagrangian acceleration measurements in stirred tank flows have not been reported previously.

2.3. Data post-processing

2.3.1. Impeller flow numbers

The impeller flow rates have been calculated, according to (2), at a distance $D/2$ from the impeller tip, that is halfway between the impeller tip and the tank wall ($r = T/3$). This choice was motivated by the following considerations. In the region very close to the impeller, the tracking efficiency, i.e. the number of obtained velocity data per volume, was low due to

the presence of the impeller and to the longer optical path of the light scattered by the tracers through the fluid. On the other hand, the extension of the impeller discharge jet diminished with the viscosity of the fluid, and in the case of cavern formation the velocity at large r was essentially null. In the literature, the flow rates are typically evaluated very close to the impeller tip ($r = T/6$). In order to account for the different radial coordinate, the flow rates have been scaled by a factor of 2. Then the flow numbers have been obtained by normalizing the flow rates by ND^3. A perfect match with the flow numbers reported in the literature is not expected, because the radial velocity decreases with the distance from the impeller. Nevertheless, this analysis allowed the effects of fluid rheology and Reynolds number on the impeller pumping capacity to be assessed.

2.3.2. Shear rate

The Lagrangian velocity data have been interpolated in a 3D Eulerian grid to obtain the mean 3D velocity fields. The grid was equi-spaced in the three Cartesian directions. This allowed the spatial derivatives of the velocity to be calculated with a centred difference scheme, and the full gradient tensor to be obtained in each node. Then, the shear rate was calculated in each node as

$$\dot{\gamma} = \sqrt{2\,\mathbf{S}{:}\,\mathbf{S}}, \tag{11}$$

where $\mathbf{S}$ is the symmetric part of the gradient. Since the non-Newtonian fluids formed pseudo-caverns and caverns, not only the shear rate distributions in the whole tank were calculated, but also those limited to an arbitrarily defined impeller region, i.e.:

$$\begin{cases} r \leq D \\ c - \dfrac{D}{4} \leq y \leq c + \dfrac{D}{4} \end{cases} \tag{12}$$

This also allowed the validity of Metzner-Otto's approach under transitional flow conditions to be assessed.

Of course, (11) is expected to underestimate the true shear rate due to the finite grid spacing, particularly in those regions at higher turbulence intensity. The grid spacing is therefore a compromise between the resolution of sharper gradients and their statistical reliability. With a 3 mm grid spacing, 87,901 nodes were used for the half tank and 7,139 nodes for the half impeller region. This allowed more than 10 velocity events to be typically binned in each cell, although a lesser number was present in some cells very close to the impeller and to the tank walls. Since the shear rate maps were determined from the mean velocities, the uncertainty associated to the shear rate was essentially due to the variance in the collections of velocity events within each cell. The standard error was selected as a metric for the shear rate uncertainty. With a 3 mm spacing, the standard error was in the order of a few percent of the shear in most of the vessel, while values close to ~10% were observed in the impeller jet, where the velocity variance was higher. In order to assess the effect of the finite spacing on the shear rate estimation, a grid of 2 mm has also been tested (293,566 nodes for the half vessel, 21,615 in the impeller region). Considering the experiment groups PL1, PL2, HB1, and NW2, the mean shear rate in the impeller region was, on average, 4.9% higher than that calculated with the 3 mm spacing; for fluid NW1, the differences between the two grids were larger (+12% to +18% with the 2 mm grid). For fluid HB2, the average shear rate was 1.6% lower using the 2 mm grid (this was probably just a binning effect, as shear decrease with grid refinement is not physically meaningful). However, with the smaller spacing, the number of velocity vectors per node obviously reduced, resulting in a few empty nodes and a noisy interpolation (over-binning). Consequently, the uncertainty in the mean velocities (hence in the shear rate) was unacceptable. For this reason, it has been decided to use the 3 mm grid. Note that the current spacing limitation is not related to PTV resolution and could be overcome by extending the size of the data set and ensuring a large number of velocity data per node. This could be achieved in many ways – one is to increase the number of recorded frames to more than 5,400.

3. Results and discussion

3.1. Flow fields visualisation

A qualitative visualisation of the investigated flows, obtained by superimposing the raw Lagrangian trajectories over four impeller revolutions, is given in Fig. 2. The white stripes represent the paths taken by the tracer particles and illustrate the overall flow patterns in the vessel. At low values of Re, the power-law fluids formed pseudo-caverns and showed low axial circulation, whereas the Herschel-Bulkley solutions formed caverns, with the flow remaining effectively stagnant outside the cavern volume.
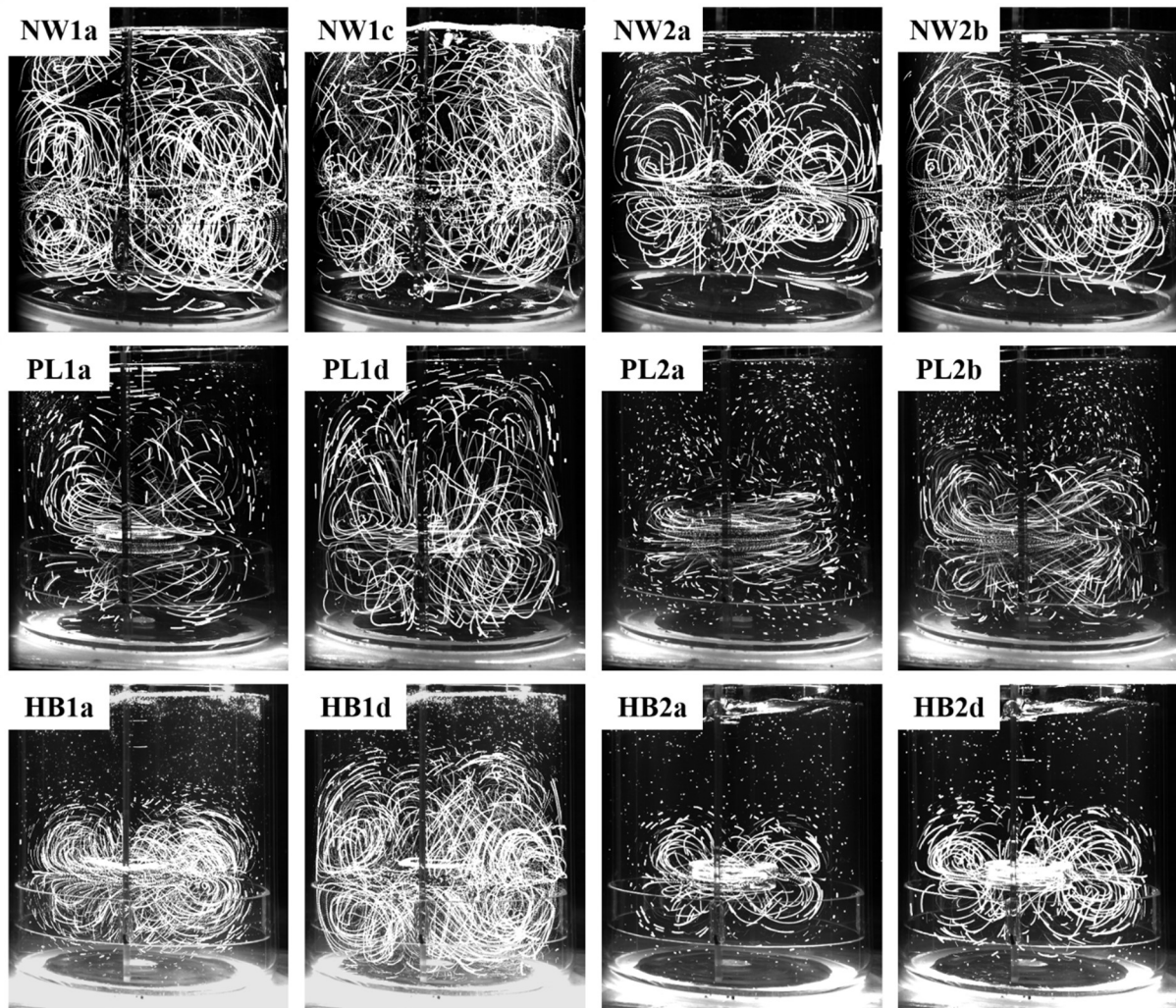
Figure 2: Tracer path lines obtained by superimposition of the raw images. The labels

indicate the experiment.

Figure 3 shows some examples of 3D trajectories obtained after PTV data processing. The colour denotes the magnitude of the velocity, normalized by the tip speed. To facilitate visualisation, only reduced samples of trajectories are shown, i.e. 5% - 8% of the original data sets. For the two Newtonian fluids, the overall flow patterns were independent of the Reynolds number in the investigated range. The tracers entering the impeller region were discharged radially and followed one of the two recirculation loops, above or below the plane of the impeller. The lower loop reached the tank bottom, while the upper loop extended to about two thirds of the vessel height. The flow interacted significantly with the tank wall and the baffles, creating systematic paths (Fig.s 3a and 3b). Such features were present in all the Reynolds numbers investigated. In the region downstream of the baffles, a small portion of fluid moved downward at low velocity (~5% of the tip speed), met the upper circulation loop and gained tangential velocity. Upstream of the baffles, the liquid flowed upwards to feed the upper circulation loop. This mechanism was responsible for the material turnover with the top of the tank. As the Reynolds number is increased, a slight increase in velocity magnitude was only observed close to walls and baffles.

With the two power-law fluids, the flow features and local velocity components changed completely with the Reynolds number. This was already visible in Fig. 2. In experiment PL1a, the near-impeller flow was almost completely tangential, with very low circulation in the radial and axial directions (Fig. 3c). In this case, the degree of agitation was not enough to maintain a substantial convection of fluid between the lower and the upper part of the tank. This was due to the shear thinning behaviour of the fluid, which dampened the momentum transfer. The extension of the impeller discharge stream, the magnitude of radial velocity in it and the intensity of the two circulation loops increased gradually with the rotational speed. The downflow behind the baffles, observed with the Newtonian fluids, was only present in experiment PL1d (Fig. 3d), but with a much smaller velocity (~1% of the tip

speed). Dead zones of low velocity were present at the top of the vessel and in the proximity of the baffles. Fig. 4a illustrates the effect of the Reynolds number on the extension of the pseudo-caverns formed by the fluids. As in the work by Adams and Barigou (2007), the boundaries have been identified as the isoline corresponding to a fluid velocity equal to 1% of the tip speed.

With the two Herschel-Bulkley fluids, the tracer particles were only tracked within the caverns around the impeller. No fluid exchange occurred with the region outside. At low Reynolds number, the fluid discharged by the impeller reached the cavern boundary and simply flowed back towards the impeller along two circulation paths, one above and one below the impeller plane (Fig. 3e). As the Reynolds number increased, the caverns expanded in size (Fig. 4b), reaching the vessel bottom and the wall (Fig. 3f). However, since the fluid at the top of the vessel was still, the downflow behind the baffles was not observed.

Since both the pseudo-cavern and cavern boundaries were defined according to the same criterion of velocity threshold, a comparison can be made between the four non-Newtonian liquids. Interestingly, different fluids showed different cavern extensions at similar Reynolds conditions (Fig. 4), indicating that the phenomenon of (pseudo-) cavern formation is rheology dependent.
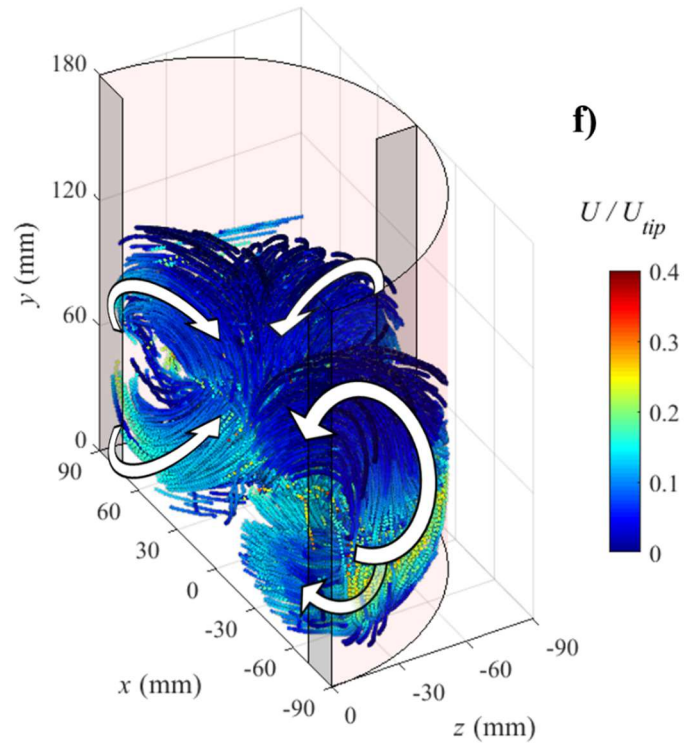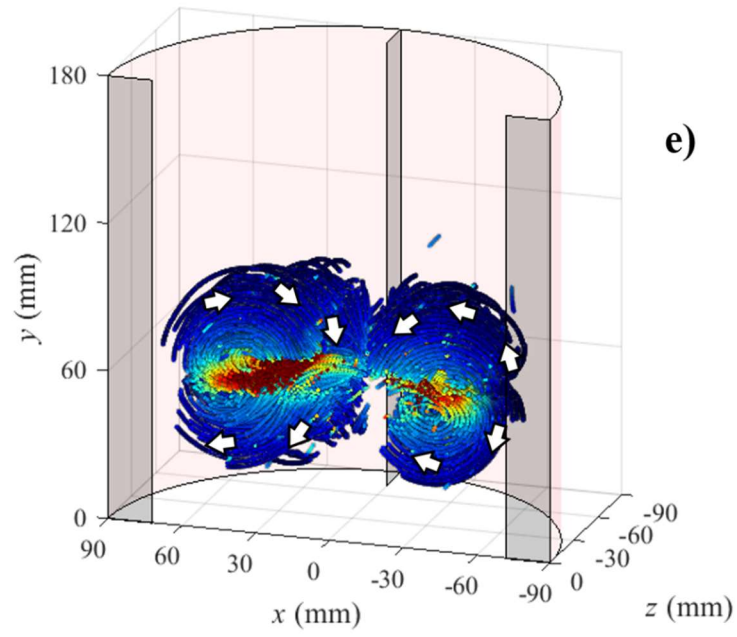
c)

d)
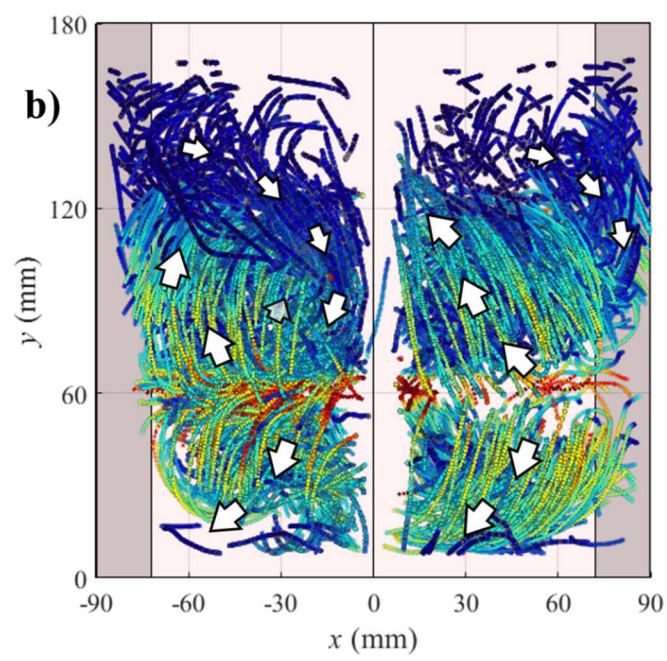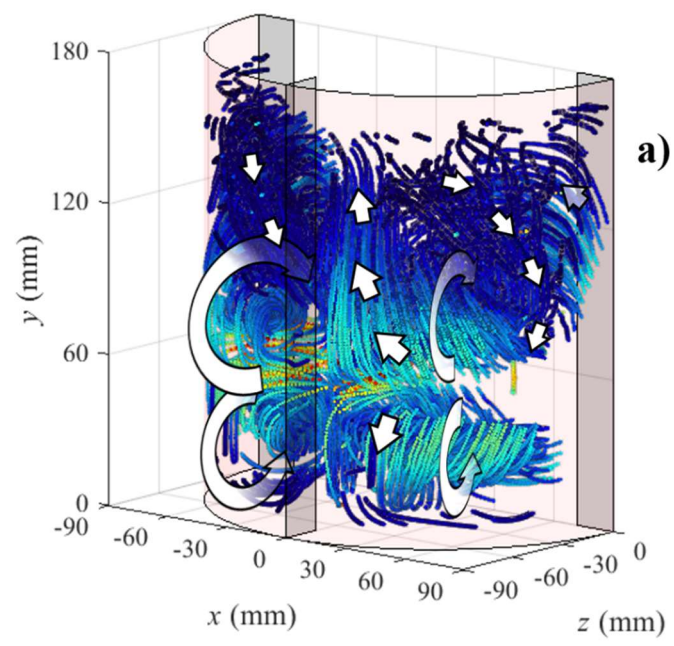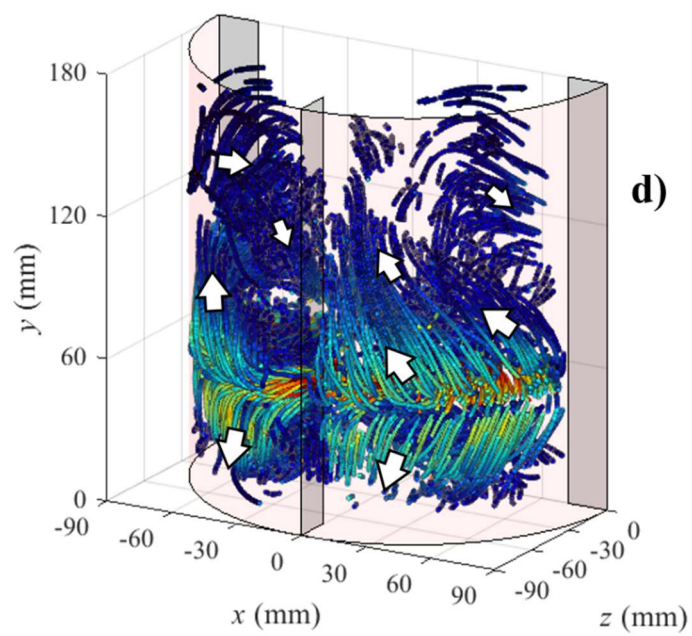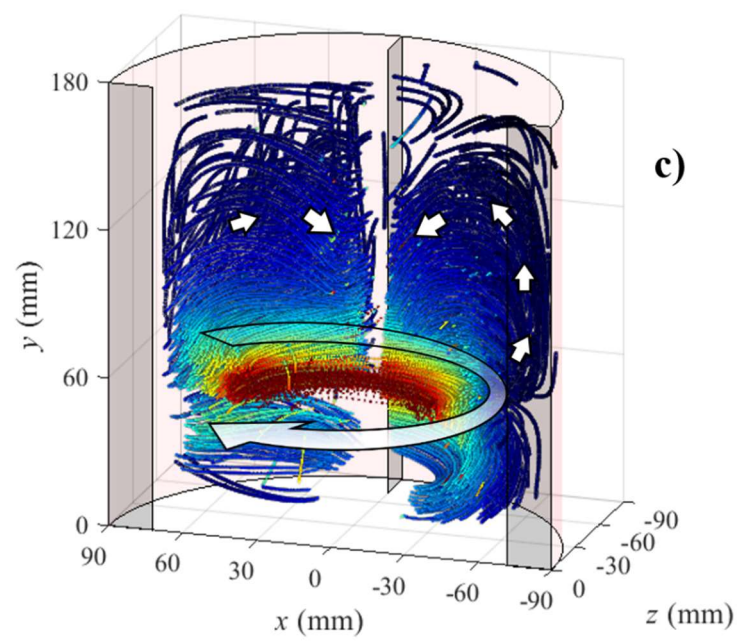
Figure 3: Examples of 3D-PTV trajectories sampled from experiments: (a) NW2b, Re = 258; (b) NW1a, Re = 629; (c), PL1a, Re = 73; (d) PL1d, Re = 1,086; (e) HB2a, Re = 151; (f) HB1c, Re = 413. The impeller rotates clockwise.

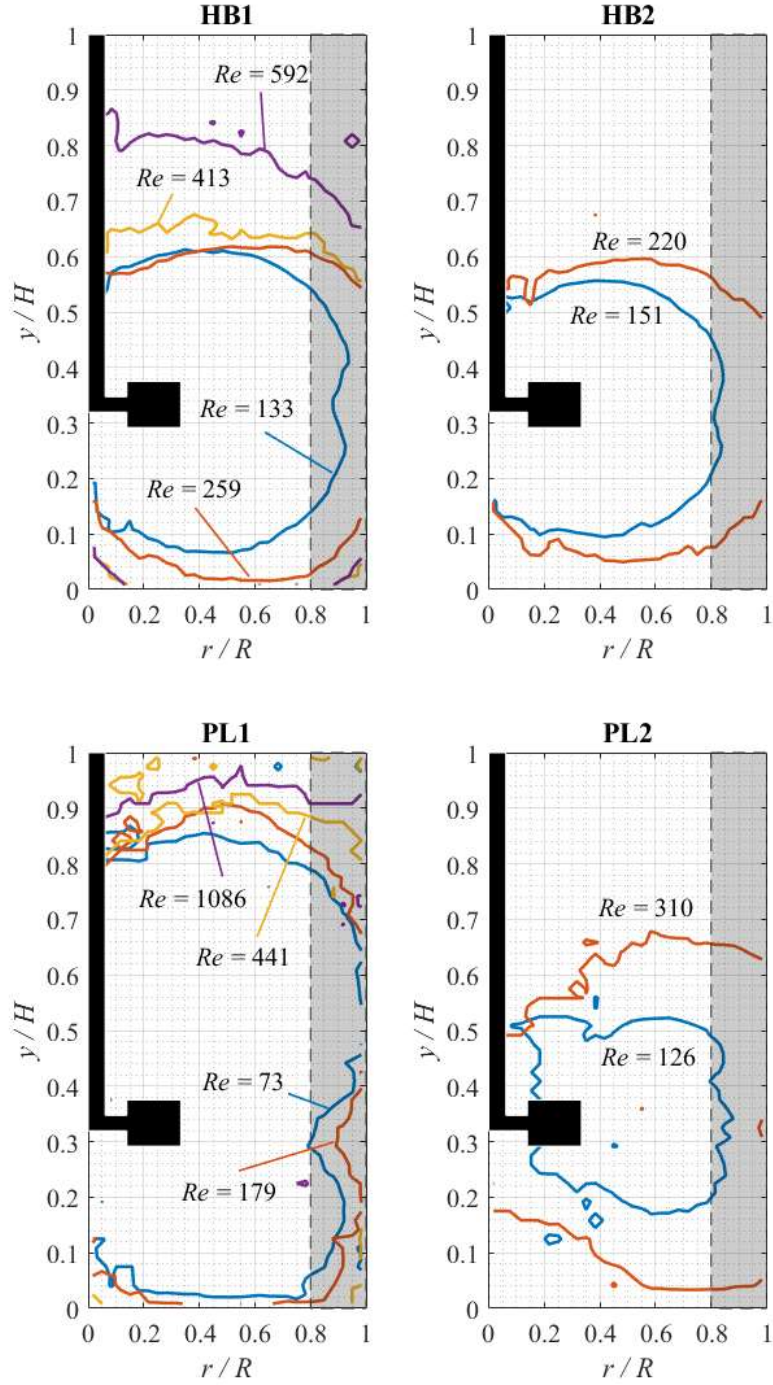*Figure 4: Pseudo-cavern and cavern boundaries as measured form PTV velocity data.*

3.2. Flow numbers

In Fig. 5a, the flow rates are plotted against the group $ND^{2.2}w(\rho/\mu_a)^{0.5}$, which was used by Norwood and Metzner (1960) to fit their measurements (3). Here $\mu_a = K\dot{\gamma}_e^{\,n-1}$ is the 'adjusted' viscosity due to shear, in which yield stress is not considered. It only differs from

the Metzner-Otto effective viscosity in the case of the yield stress fluids. The reason for this modification is that the flowing fluid does not experience the effects of the yield stress, hence the volumetric flow rate only depends on shear rate. The proportionality fitting in Fig. 5a gave a coefficient of determination of 0.76, which is reasonably high for 17 experimental measurements at various conditions. Fig.5b shows the flow numbers measured against the adjusted Reynolds number, $Re_a = \rho D^2 N / \mu_a$. Since the flow rates were calculated at $r = T/3$ instead of the typical $r = T/6$, the values of flow number were slightly lower than those reported in the literature. Nevertheless, their trends were very informative. For the Newtonian fluids, the flow number was weakly dependent on Re_a. A power-law fitting indicated that Fl scaled as $Re_a{}^{0.036}$. Non-Newtonian fluids were characterized by smaller flow numbers than Newtonian fluids. In the left region, for $Re_a < {\sim}400$, Fl increased as $Re_a{}^{1.1}$. For $Re_a > {\sim}400$, Fl was proportional to $Re_a{}^{0.23}$, approaching the curve of the Newtonian fluids. The exponents agree with those obtained by Koutsakos and Nienow (1990) and Dyster et al. (1993), indicating that the decrease in radial velocity from $r = T/6$ to $r = T/3$ was consistent across the different experiments. Flow number data, together with previous observations, suggest that a gradual change in the non-Newtonian flow dynamics occurred around $Re{\sim}400$, due to the incipient interactions between the inner flow around the impeller and the outer flow close to the baffles and walls. In a previous study using DNS data (Tamburini et al., 2018), the same mechanism was evoked to explain the gradual transition from laminar to turbulent flow, in the range of Re between 150 and 600, and the different behaviour the flow between baffled and unbaffled vessels. It can be concluded that the Rushton capacity to pump a non-Newtonian fluid around the vessel becomes very poor below $Re{\sim}400$ and practitioners should take into considerations different geometries for those mixing conditions.
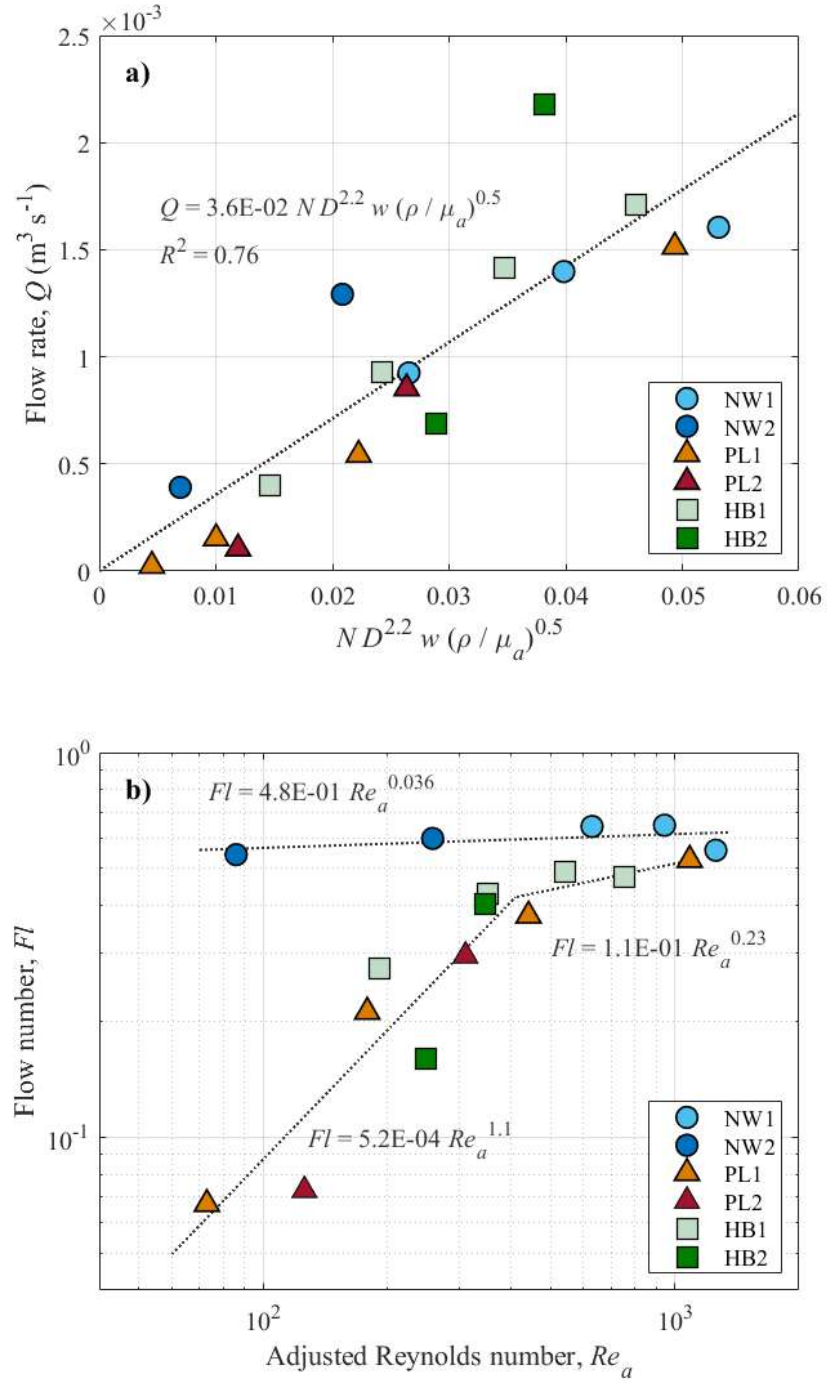
a)

$Q = 3.6\text{E-}02\ N D^{2.2}\ w\ (\rho\,/\,\mu_a)^{0.5}$

$R^2 = 0.76$

b)

$Fl = 4.8\text{E-}01\ Re_a{}^{0.036}$

$Fl = 1.1\text{E-}01\ Re_a{}^{0.23}$

$Fl = 5.2\text{E-}04\ Re_a{}^{1.1}$

Figure 5: Fitting of the flow rates against Norwood and Metzner's correlation group (a) and impeller flow number against Reynolds number (b).

3.3. Shear rate and Lagrangian acceleration

In all the experiments, both the shear rate and the Lagrangian acceleration were distributed in logarithmic space, spanning different orders of magnitude. This reflects the variety of fluid dynamics conditions at different locations within the vessel.

The shear rate was higher in the region surrounding the impeller, and the differences with the overall distribution were particularly significant with the non-Newtonian fluids (Figs. 6a-c and 7a), due to the larger spatial variability of the flows. In the case of Newtonian fluids, the shear rate was distributed log-normally both in the impeller region and in the entire vessel. It being understood that the shear decreased with the distance from the impeller, this transition was smooth, and the fluid remained sufficiently and uniformly sheared also in the bulk, where $\dot{\gamma} \sim N$. Instead, the distributions of the non-Newtonian fluids in the entire vessels tended towards bimodality, due to pseudo-cavern and cavern formation. Shear rate decreased very quickly – more than one order of magnitude – close to the (pseudo-) cavern boundary. With the power law fluids, the flow occurred even outside of the pseudo-caverns, that is a significant fraction of the vessel volume, albeit with very low velocities and shear ($\dot{\gamma} \sim 10^{-1} N$). Instead, with the Herschel-Bulkley fluids, very low shear was confined close to the cavern boundary. As anticipated in §2.3.2, the standard error associated to the shear rate maps was in the order of a few percent in most of the tank and about ~10% in the impeller discharge region, due to the higher velocity variance there. These values could be reduced by increasing the size of the datasets. One example of error map is pictured in Fig.6d. Three examples of shear distributions are illustrated in Fig. 7a. Clearly, the curves were dependent on fluid rheology for the reasons discussed above. However, the means of the curves were relatively close, therefore some fitting models were attempted. The analysis focused on the impeller region because of its importance to the mixing process and to assess the validity of Metzner-Otto's assumption. Considering all working fluids, the best power-law fitting of the average shear rate against the impeller

rotational speed gave an exponent of 1.08 (Fig. 8a). The bars in Fig. 8 represent one standard deviation of the individual shear distributions in logarithmic space, therefore they should not be intended as confidence intervals (due to the large data sets, the standard error of the mean was extremely small). A simple proportionality law, i.e. $\langle \dot{\gamma} \rangle = 6.1 \, N$, still predicts the mean shear rate characterising the near-impeller flow with reasonable accuracy ($R^2 = 0.85$). As already discussed, the value of the proportionality constant, $k_s^* = 6.1$, depends on the volume and shape of the impeller region, which was defined arbitrarily. The impeller region used in this paper is comparable to the control volume labelled 'ESV' in the work by Ramírez-Muñoz et al. (2017), although some differences were present. The exact dimensions of ESV were not reported (ESV appears smaller than the impeller region here), their tank had a curved bottom and the flow regime was laminar. In ESV, Ramírez-Muñoz et al. measured $k_s^* = 7.2$.

The high coefficients of determination ($R^2 = 0.92$ and $R^2 = 0.85$) of the 'all-fluids' fittings suggest that rheology effects, if present, were small compared to the variation of shear rate attributable to the impeller speed. However, the shear rate measured with the Newtonian fluids was systematically higher than with non-Newtonian fluids, N being the same. For this reason, the data have been categorised as Newtonian or non-Newtonian and two additional fittings have been calculated separately (Fig. 8a). Indeed, these have higher coefficient of determination than the overall fittings, meaning that the classification into two subsets based on fluid rheology has helped explain a larger share of variance in the data. In the case of Newtonian fluids, $k_s^* = 8.4$ ($R^2 = 0.94$), while $k_s^* = 5.6$ ($R^2 = 0.97$) for the non-Newtonian fluids. Further to this analysis, a dependency of $k_s^* = \langle \dot{\gamma} \rangle / N$ on Re was also tested (Fig. 8b). Again, Newtonian and non-Newtonian data were fitted separately (13a and 13b). A linear model was chosen because k_s^* is expected to become constant in the limit of low Re, that is under fully laminar conditions.

$$\langle \dot{\gamma} \rangle_N = (6.8 + 2.0 \cdot 10^{-3} \, Re) \, N; \tag{13a}$$

$$\langle \dot{\gamma} \rangle_{NN} = (4.8 + 1.6 \cdot 10^{-3} \, Re) \, N. \tag{13b}$$

In the first case, the predicted normalised shear rate changed from 6.9 to 9.3 in the range of Re between 86 (experiment NW2a) and 1,257 (NW1c). With the non-Newtonian fluids, the predicted k_s^* changed from 4.9 to 6.5 in the range of Re between 73 (experiment PL1a) and 1,086 (PL1d). Numerically, the effects of the Reynolds number become increasingly significant when $Re > \sim 300$. This reflects the gradual deviation from Metzner-Otto's scaling rule as Reynolds number increases. Note that the coefficients of determination of (13a) and (13b) refer to the residual variance in the data, once the variation of shear due to the impeller speed has already been accounted for by fitting $\langle \dot{\gamma} \rangle / N$ as a dependent variable.
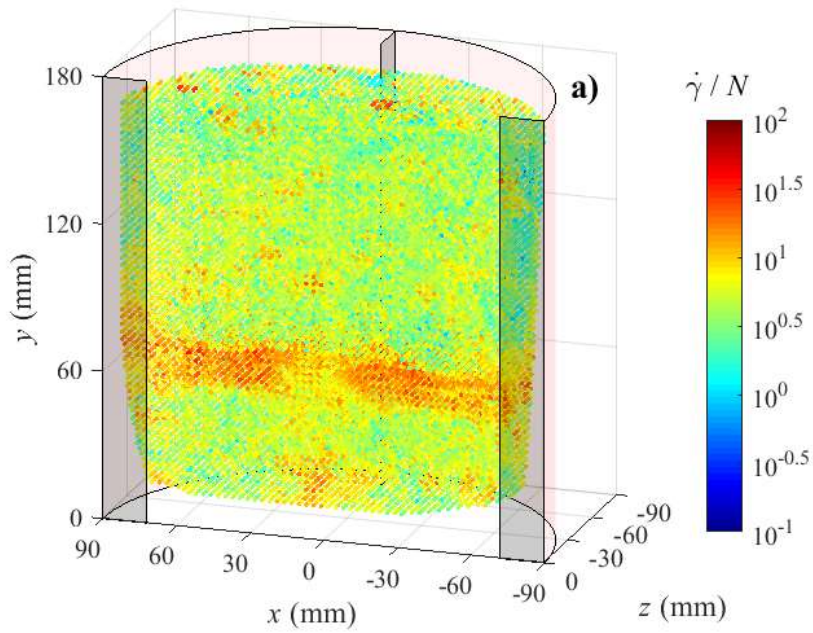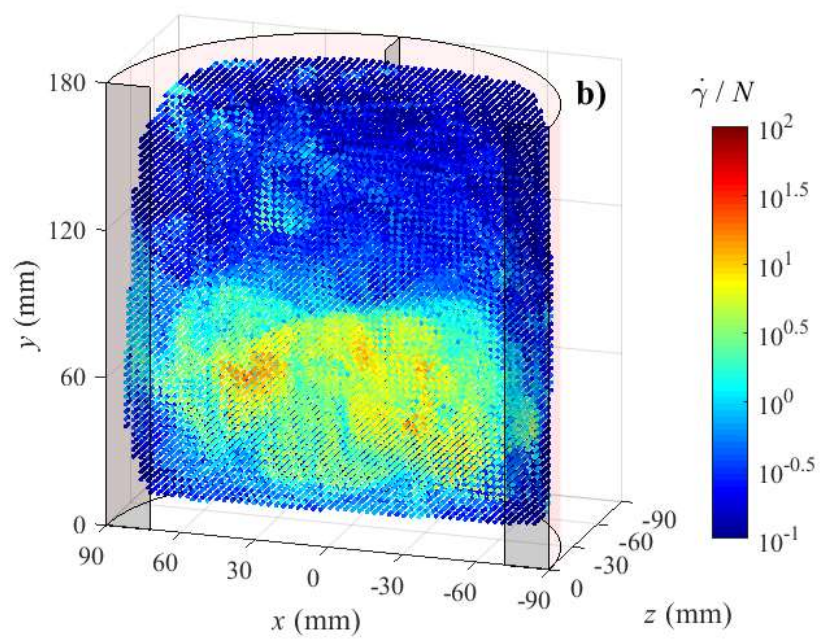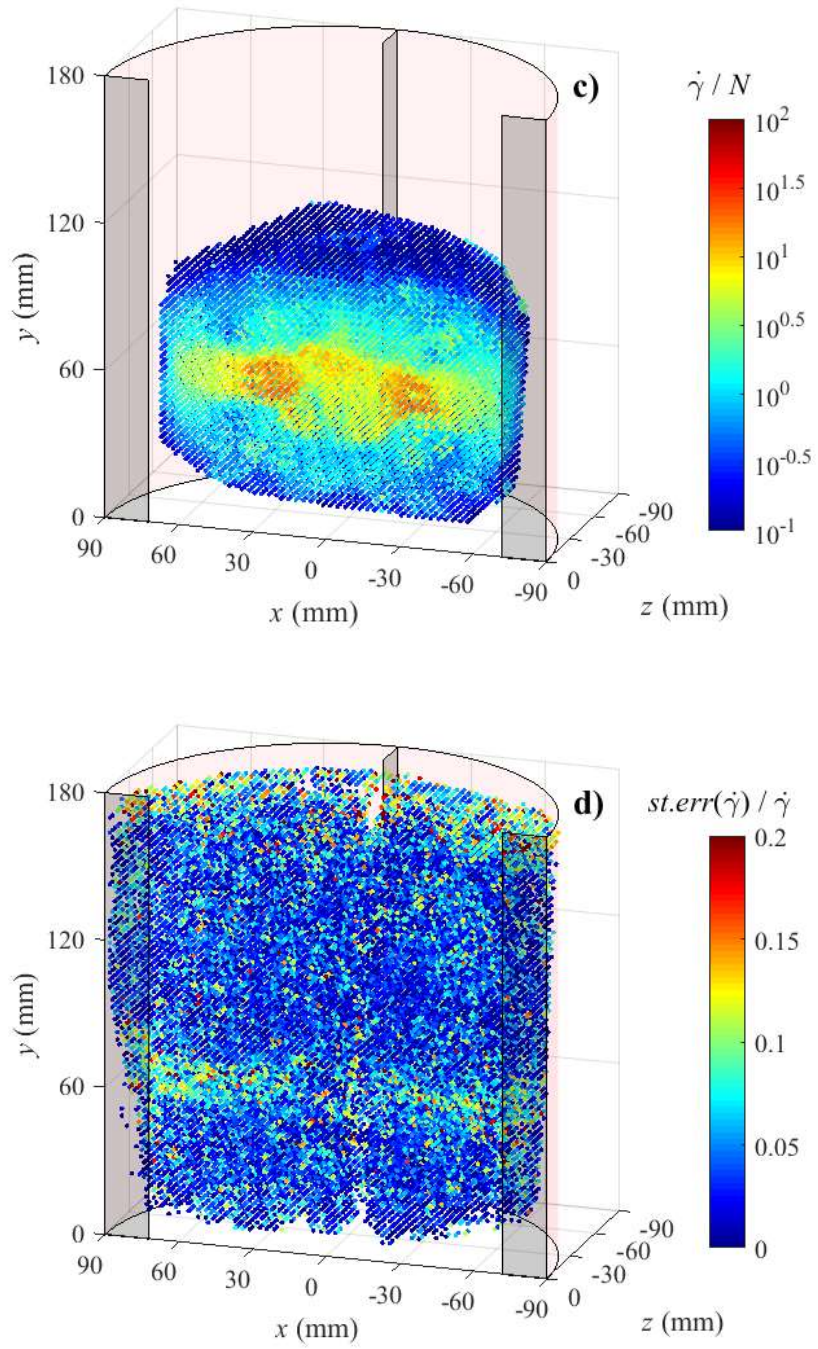
Figure 6: Examples of normalised shear rate maps in the vessel. (a) experiment NW1c; (b) experiment PL2a; (c) experiment HB2a. Subfigure (d) shows the standard error of the shear rate for experiment NW1c.
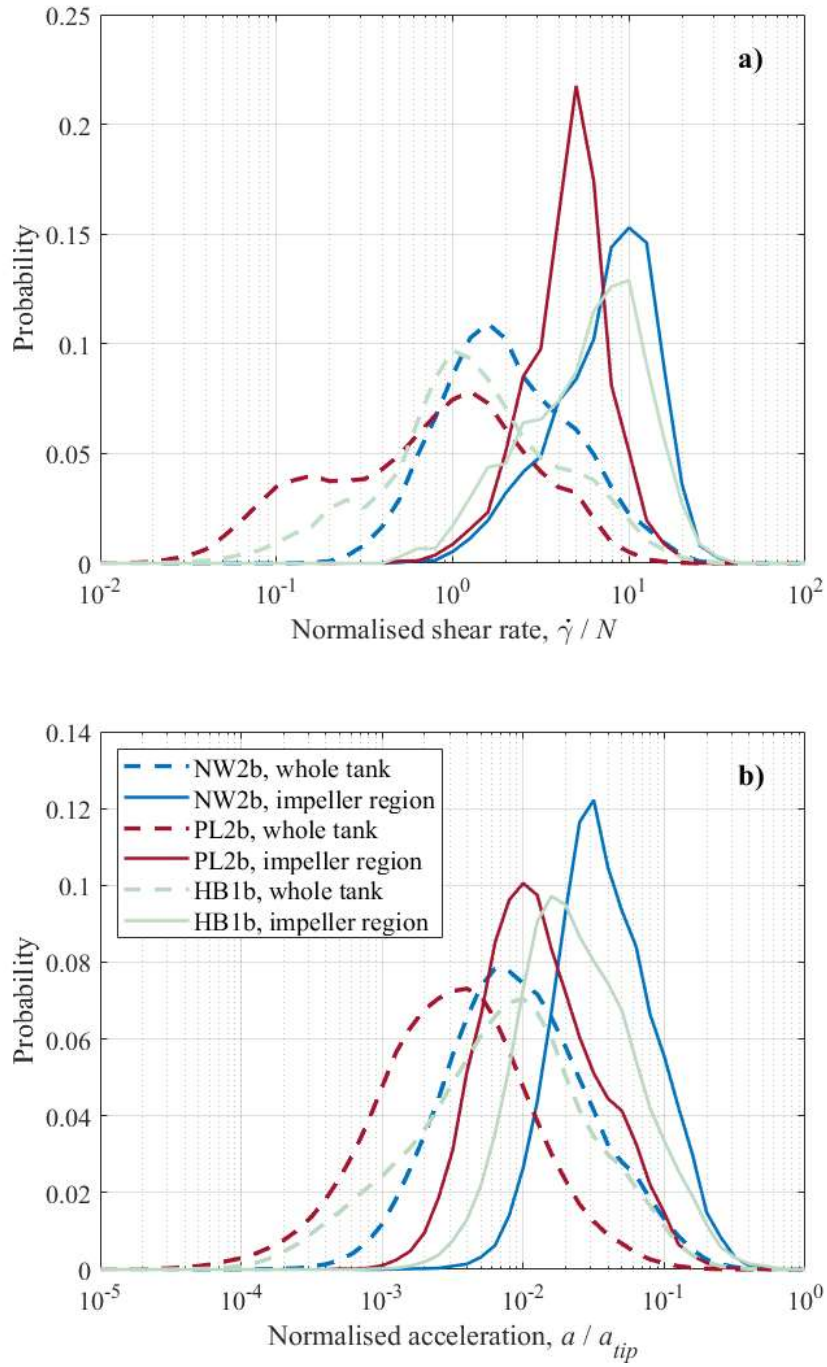
Figure 7: Examples of distributions of normalised shear rate (a) and Lagrangian acceleration (b) for three experiments at comparable Reynolds number.
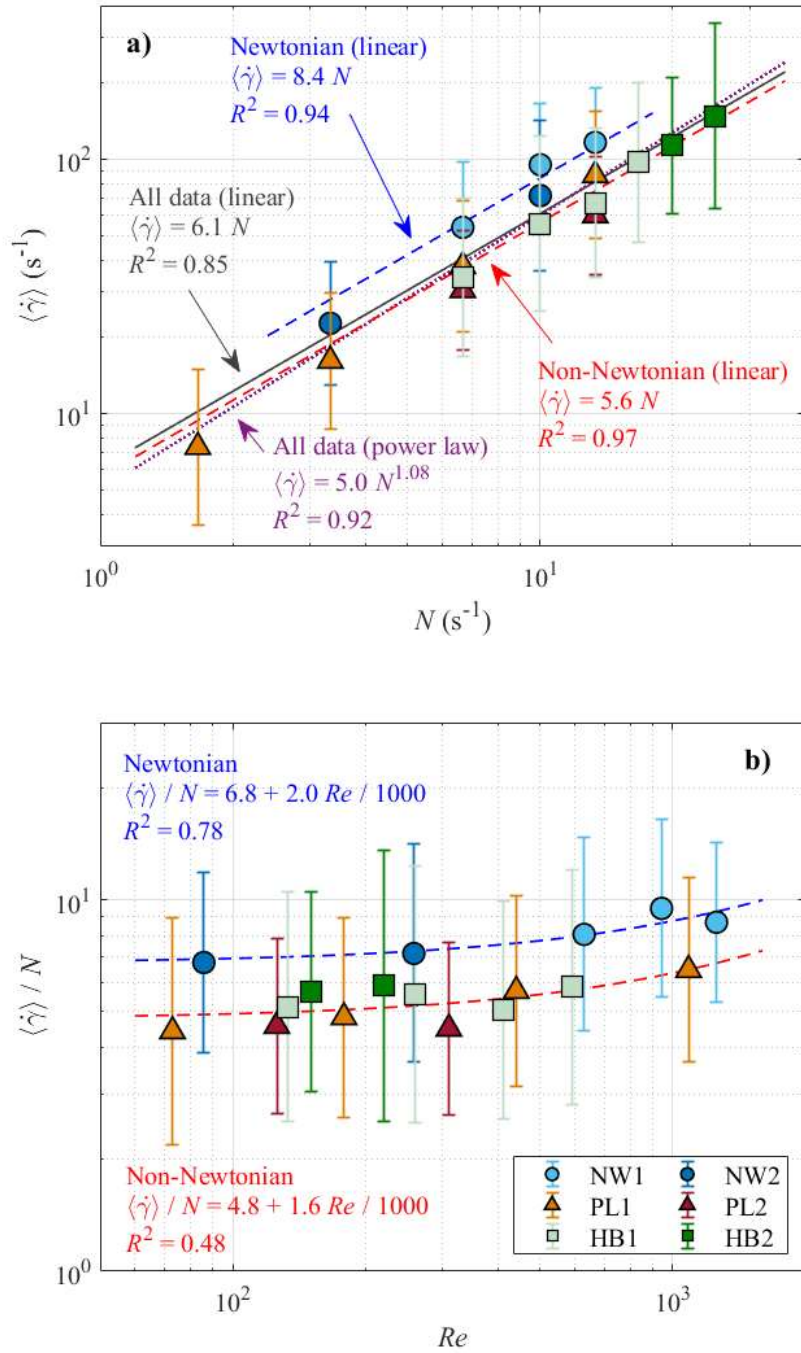
Figure 8: Average shear rate in the impeller region against the impeller speed (a) and its ratio over the impeller speed against the Reynolds number (b).

Three examples of acceleration distribution, normalised with the centripetal acceleration at the impeller tip, $a_{tip} = 2\,U_{tip}{}^2/D$, are pictured in Fig. 7b. The distributions were approximately log-normal. The mean acceleration in the impeller region was one or more

orders of magnitude larger than in the entire vessel. In the impeller region, the average Lagrangian acceleration scaled with the average shear rate to the power of 1.8 (Fig. 9). The coefficient of determination of the fitting was $R^2 = 0.96$. The high degree of correlation between the two quantities has two important implications. First, acceleration, which is easily measured with 3D-PTV, can be used as an indicator of the local degree of mixing, similarly to shear rate. This eliminates the difficulties related to PTV data interpolation when estimating the shear rate. Secondly, like for the shear rate, the forces acting on the fluid elements are determined by the impeller speed, the Reynolds number and the fluid rheology in combination. Therefore, practitioners should take into consideration that transitional flows at the same Reynolds number are not necessarily dynamically equivalent. Further work should be conducted to assess whether this is true also in the laminar and fully turbulent regimes.
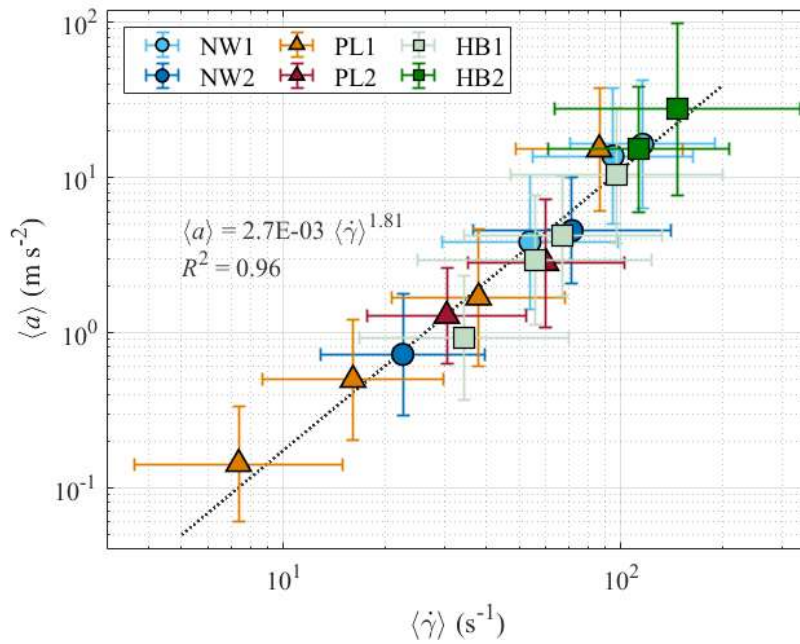

Figure 9: Average Lagrangian acceleration against average shear rate in the impeller region.

4. Conclusions

In this paper, the flow fields of six fluids in a 4.6 L cylindrical tank stirred with a Rushton turbine and operated in the transitional regime (Re from 73 to 1,257) have been measured by means of 3D-PTV. The working fluids had different rheology, namely Newtonian, shear-thinning and Herschel-Bulkley.

Newtonian fluids showed very similar flow patterns in the range of Reynolds number from 86 to 1,257. Non-Newtonian flow patterns changed dramatically in the range of Reynolds number investigated. Non-Newtonian fluids formed pseudo-caverns and caverns around the impeller, the size of which was rheology dependent and increased with Reynolds. The impeller flow numbers have been calculated from azimuthally averaged radial velocity data. For practical reasons, they have been evaluated at a radial coordinate $r = T/3$ instead of $r = T/6$ (impeller tip). For the Newtonian fluids, the flow number was almost constant (0.6 on average) in a range of Reynolds from 86 to 1,257. With the non-Newtonian fluids, two separate trends were observed. Fl scaled as $Re^{1.1}$ for $Re < {\sim}400$ and as $Re^{0.23}$ for $Re > {\sim}400$. Non-Newtonian rheology significantly decreased the impeller's capacity to pump the fluid in the vessel when $Re < {\sim}400$. Low fluid circulation and (pseudo-) cavern formation have detrimental effects on macromixing. High impeller velocities could potentially guarantee substantial flow in the whole vessel. However, the resulting power drawn would be too high for industrial purposes. Close-clearance impellers, such as anchors and ribbons, could be a better solution for non-Newtonian fluid agitation at low Reynolds.

The shear rate maps have been obtained by interpolating the velocity vectors in a Cartesian grid. The shear rate distributions were approximately log-normal. For practical purposes, the volume-averaged shear in the impeller region can be assumed to scale as $\langle \dot{\gamma} \rangle = 6.1\,N$ with reasonable accuracy ($R^2 = 0.85$). This proportionality law clearly resembles the Metzner-Otto's assumption, valid in the laminar regime. The model has been refined by fitting

Newtonian and non-Newtonian shear data separately and by expressing k_s^* as a function of the Reynolds number. This accounts for rheology effects and reflects the growing contribution of turbulence to shear generation as the flow deviates from fully laminar conditions. Equations (13a) or (13b) can be used by practitioners to predict the mean shear conditions of a mixing process in the transitional regime, with higher accuracy than a simple proportionality law. However, it is important to remember that (a) the value of all fitting parameters depend on the volume and shape of the impeller region, which was defined arbitrarily, thus consistent procedures must be adopted when comparing different mixing systems, (b) individual shear rate realisations may be much greater or smaller than the mean, because this quantity is distributed over many orders of magnitude and (c) fluid rheology strongly affects the shear distribution in the vessel (with power-law fluids, the shear can be $\dot{\gamma} \sim 10^{-1} \, N$ in a substantial fraction of the vessel volume).

Lagrangian acceleration was also distributed log-normally within the vessel. In the impeller region, the mean acceleration scaled as the volume-averaged shear to the power of 1.8 ($R^2 = 0.96$). This suggests that acceleration, measured directly with PTV, is a good indicator of local mixing intensity.

To the authors' knowledge, this is the first publication in which PTV is used to study stirred tank flows in a wide range of experimental conditions. Current knowledge has been confirmed with very simple hardware, and this might be extremely relevant for industrial R&D sectors with limited access to advanced experimental facilities. Furthermore, PTV data have provided unique information regarding the local fluid acceleration in the vessel, which has been rarely reported in the literature and is not accessible by means of traditional Eulerian techniques, such as PIV and LDV.

Appendix: Statistical convergence of the measurements

The statistical convergence of the velocity measurements has been validated by monitoring its ensemble average and ensemble standard deviation in three sample volumes as a function of the number of events, m. The average velocity was calculated as

$$\langle U \rangle_m = \frac{1}{m} \sum_{i=1}^{m} U_i \tag{14}$$

and the standard deviation as

$$\sigma_m = \sqrt{\frac{1}{m-1} \sum_{i=1}^{m} (U_i - \langle U \rangle_m)^2} \; . \tag{15}$$

Here the index i indicates the individual observations. The sample volumes were semi-annular voxels of volume $V_s = 0.1\% \, (V_{tank}/2) = 2.3 \text{ cm}^3$ (Fig. 10). The first was placed in the impeller discharge region at $r = T/4 \pm 2$ mm, $y = H/3 \pm 2$ mm. The second was close to the wall, at $r = (T - b)/2 \pm 1.5$ mm, $y = H/2 \pm 1.5$ mm. The third was in the bulk of the flow, at $r = T/3 \pm 1.75$ mm, $y = 2H/3 \pm 1.75$ mm. With some of the Herchel-Bulkley flows, the sample volumes had to be placed differently, because of the caverns. In all experiments, both the average and the standard deviation were independent by the number of events. One example of such plots is given in Fig.11. The standard deviation was higher in the impeller region and changed between different flows depending on the Reynolds number. Note that the standard deviation does not correspond to the root-mean-square turbulent velocity, because the flow tracers were too large to resolve the flow turbulent scales.
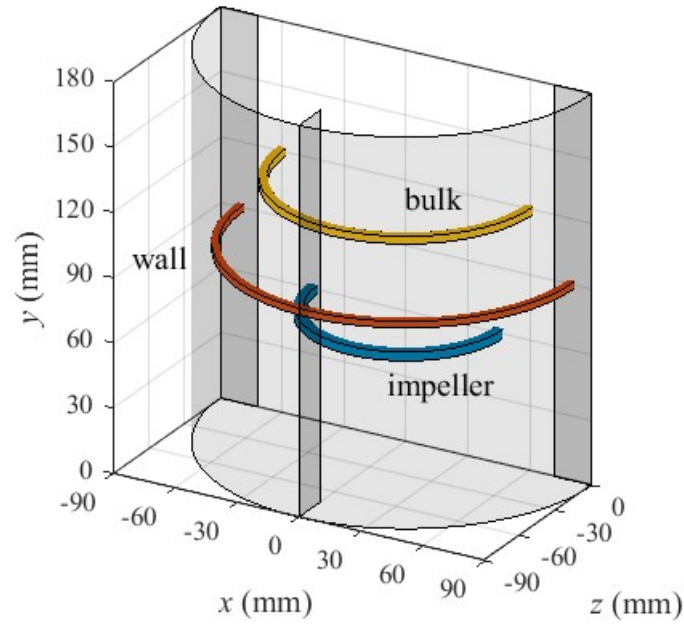
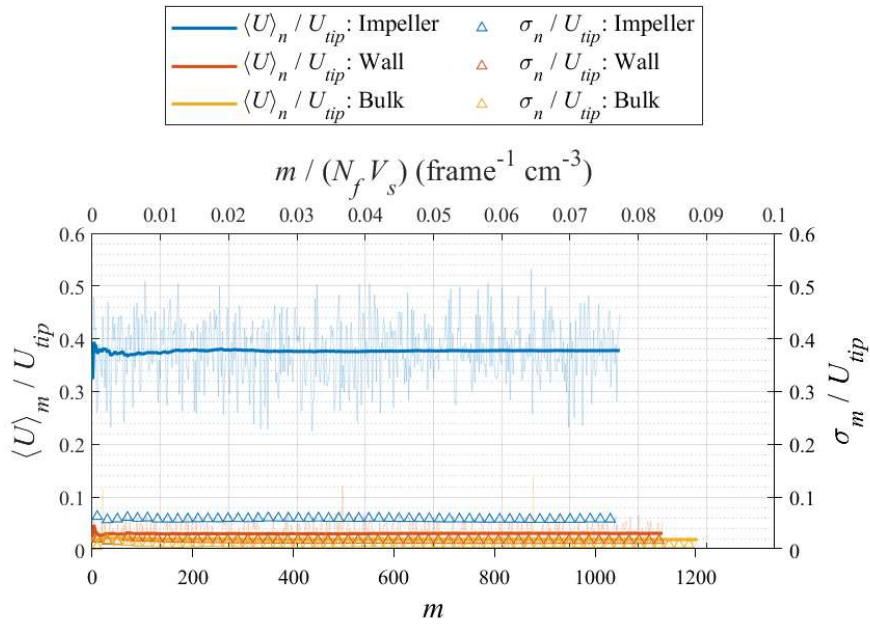*Figure 10: Position of the sample volumes in the vessel.*

Figure 11: Ensemble average and standard deviation of the velocity in the sample volume

(data from experiment PL1c).

Acknowledgments

References

Adams, L.W., Barigou, M., 2007. CFD Analysis of Caverns and Pseudo-Caverns Developed During Mixing of Non-Newtonian Fluids. Chem. Eng. Res. Des. 85, 598–604. https://doi.org/10.1205/cherd06170

Aguirre-Pablo, A.A., Aljedaani, A.B., Xiong, J., Idoughi, R., Heidrich, W., Thoroddsen, S.T., 2019. Single-camera 3D PTV using particle intensities and structured light. Exp. Fluids 60, 25. https://doi.org/10.1007/s00348-018-2660-7

Alberini, F., Liu, L., Stitt, E.H., Simmons, M.J.H., 2017. Comparison between 3-D-PTV and 2-D-PIV for determination of hydrodynamics of complex fluids in a stirred vessel. Chem. Eng. Sci. 171, 189–203. https://doi.org/10.1016/j.ces.2017.05.034

Ameur, H., Bouzit, M., 2012. Mixing in shear thinning fluids. Braz. J. Chem. Eng. 29, 349–358. https://doi.org/10.1590/S0104-66322012000200015

Anne-Archard, D., Marouche, M., Boisson, H.-C., 2006. Hydrodynamics and Metzner-Otto correlation in stirred vessels for yield stress fluids. Chem. Eng. J. 125, 15–24. https://doi.org/10.1016/j.cej.2006.08.002

Barnes, H.A., Hutton, J.F., Walters, K. (Eds.), 1989. Chapter 2 - Viscosity, in: An Introduction to Rheology, Rheology Series. Elsevier, Oxford, UK, pp. 11–35. https://doi.org/10.1016/B978-0-444-87469-6.50006-8

Beckner, J.L., Smith, J.M., 1966. Anchor-Agitated Systems: PowerInput With Newtonian and Pseudo-Plastic Fluids. Trans. IChemE 44, 224–236.

Bertrand, F., Tanguy, P.A., Fuente, E.B.-D.L., 1996. A New Perspective for the Mixing of Yield Stress Fluids with Anchor Impellers. J. Chem. Eng. Jpn. 29, 51–58. https://doi.org/10.1252/jcej.29.51

Böhme, G., Stenger, M., 1988. Consistent scale-up procedure for the power consumption in agitated non-newtonian fluids. Chem. Eng. Technol. 11, 199–205. https://doi.org/10.1002/ceat.270110127

Cabaret, F., Fradette, L., Tanguy, P.A., 2008. New Turbine Impellers for Viscous Mixing. Chem. Eng. Technol. 31, 1806–1815. https://doi.org/10.1002/ceat.200800385

Calderbank, P.H., Moo-Young, M.B., 1961. The Power Characteristics of Agitators for the Mixing of Newtonian and Non-Newtonian Fluids. Trans. IChemE 39, 337–347.

Chiti, F., Bakalis, S., Bujalski, W., Marigo, M., Eaglesham, A., Nienow, A., 2011. Using positron emission particle tracking (PEPT) to study the turbulent flow in a baffled vessel agitated by a Rushton turbine: Improving data treatment and validation. Chem. Eng. Res. Des. 89, 1947–1960. https://doi.org/10.1016/j.cherd.2011.01.015

Dickey, D.S., 2015. Tackling Difficult Mixing Problems. Chem. Eng. Prog. 35–42.

Distelhoff, M.F.W., Laker, J., Marquis, A.J., Nouri, J.M., 1995. The application of a strain gauge technique to the measurement of the power characteristics of five impellers. Exp. Fluids 20, 56–58. https://doi.org/10.1007/BF00190598

Doraiswamy, D., Grenville, R.K., Etchells, A.W., 1994. Two-Score Years of the Metzner-Otto Correlation. Ind. Eng. Chem. Res. 33, 2253–2258. https://doi.org/10.1021/ie00034a001

Dyster, K.N., Koutsakos, E., Jaworski, Z., Nienow, A.W., 1993. An LDA study of the radialdischarge velocities generated by a Rushton turbine: Newtonian Fluids, Re>=5. Trans. IChemE 71, 11–23.

Gallo, D., Gülan, U., Di Stefano, A., Ponzini, R., Lüthi, B., Holzner, M., Morbiducci, U., 2014. Analysis of thoracic aorta hemodynamics using 3D particle tracking velocimetry and computational fluid dynamics. J. Biomech. 47, 3149–3155. https://doi.org/10.1016/j.jbiomech.2014.06.017

Greenville, R.K., 1992. Blending of Viscous Newtonian and Pseudo-Plastic FLuids (PhD Thesis). Cranfield Institute of Technology, Cranfield, UK.

Gülan, U., Lüthi, B., Holzner, M., Liberzon, A., Tsinober, A., Kinzelbach, W., 2012. Experimental study of aortic flow in the ascending aorta via Particle Tracking Velocimetry. Exp. Fluids 53, 1469–1485. https://doi.org/10.1007/s00348-012-1371-8

Hemrajani, R.R., Tatterson, G.B., 2004. Mechanically Stirred Vessels, in: Handbook of Industrial Mixing. John Wiley & Sons, Ltd, Hoboken, N.J., US, pp. 345–390. https://doi.org/10.1002/0471451452.ch6

Holzner, M., Liberzon, A., Nikitin, N., Lüthi, B., Kinzelbach, W., Tsinober, A., 2008. A Lagrangian investigation of the small-scale features of turbulent entrainment through particle tracking and direct numerical simulation. J. Fluid Mech. 598, 465–475. https://doi.org/10.1017/S0022112008000141

Israel, R., Rosner, D.E., 1982. Use of a Generalized Stokes Number to Determine the Aerodynamic Capture Efficiency of Non-Stokesian Particles from a Compressible Gas Flow. Aerosol Sci. Tech. 2, 45–51. https://doi.org/10.1080/02786828308958612

Jahangiri, M., Golkar-Narenji, M.R., Montazerin, N., Savarmand, S., 2001. Investigation of the viscoelastic effect on the Metzner and Otto coefficient through LDA velocity measurements. Chin. J. Chem. Eng. 9, 77–83.

Kelly, W., Gigas, B., 2003. Using CFD to predict the behavior of power law fluids near axial-flow impellers operating in the transitional flow regime. Chem. Eng. Sci. 58, 2141–2152. https://doi.org/10.1016/S0009-2509(03)00060-5

Kinzel, M., Wolf, M., Holzner, M., Lüthi, B., Tropea, C., Kinzelbach, W., 2010. Simultaneous two-scale 3D-PTV measurements in turbulence under the influence of system rotation. Exp. Fluids 51, 75–82. https://doi.org/10.1007/s00348-010-1026-6

Koutsakos, E., Nienow, A.W., Dyster, K.N., 1990. Laser Anemometry study of shear thinning fluids agitated by a Rushton turbine. IChemE Symp., Series 121 121, 51–73.

Krug, D., Holzner, M., Lüthi, B., Wolf, M., Tsinober, A., Kinzelbach, W., 2014. A combined scanning PTV/LIF technique to simultaneously measure the full velocity gradient tensor and the 3D density field. Meas. Sci. Technol. 25, 065301. https://doi.org/10.1088/0957-0233/25/6/065301

Krug, D., Lüthi, B., Seybold, H., Holzner, M., Tsinober, A., 2012. 3D-PTV measurements in a plane Couette flow. Exp. Fluids 52, 1349–1360. https://doi.org/10.1007/s00348-011-1256-2

Kukukova, A., Aubin, J., Kresta, S.M., 2011. Measuring the scale of segregation in mixing data. Can. J. Chem. Eng. 89, 1122–1138. https://doi.org/10.1002/cjce.20532

Liberzon, A., Lüthi, B., Holzner, M., Ott, S., Berg, J., Mann, J., 2012. On the structure of acceleration in turbulence. Physica D 241, 208–215. https://doi.org/10.1016/j.physd.2011.07.008

Lüthi, B., Tsinober, A., Kinzelbach, W., 2005. Lagrangian measurement of vorticity dynamics in turbulent flow. J. Fluid Mech. 528, 87–118. https://doi.org/10.1017/S0022112004003283

Maas, H.G., Gruen, A., Papantoniou, D., 1993. Particle tracking velocimetry in three-dimensional flows. Exp. Fluids 15, 133–146. https://doi.org/10.1007/BF00190953

Machado, M.B., Bittorf, K.J., Roussinova, V.T., Kresta, S.M., 2013. Transition from turbulent to transitional flow in the top half of a stirred tank. Chem. Eng. Sci.

Malik, N.A., Dracos, Th., Papantoniou, D.A., 1993. Particle tracking velocimetry in three-dimensional flows. Exp. Fluids 15, 279–294. https://doi.org/10.1007/BF00223406

Márquez-Baños, V.E., De La Concha-Gómez, A.D., Valencia-López, J.J., López-Yáñez, A., Ramírez-Muñoz, J., 2019. Shear rate and direct numerical calculation of the Metzner-Otto constant for a pitched blade turbine. J. Food Eng. 257, 10–18. https://doi.org/10.1016/j.jfoodeng.2019.03.021

McKeon, B., Comte-Bellot, G., Foss, J., Westerweel, J., Scarano, F., Tropea, C., Meyers, J., Lee, J., Cavone, A., Schodl, R., Koochesfahani, M., Andreopoulos, Y., Dahm, W., Mullin, J., Wallace, J., Vukoslavčević, P., Morris, S., Pardyjak, E., Cuerva, A., 2007. Velocity, Vorticity, and Mach Number, in: Tropea, C., Yarin, A.L., Foss, J.F. (Eds.), Springer Handbook of Experimental Fluid Mechanics, Springer Handbooks. Springer, Berlin, Heidelberg, Germany, pp. 215–471. https://doi.org/10.1007/978-3-540-30299-5_5

Mendoza, F., Bañales, A.L., Cid, E., Xuereb, C., Poux, M., Fletcher, D.F., Aubin, J., 2018. Hydrodynamics in a stirred tank in the transitional flow regime. Chem. Eng. Res. Des. 132, 865–880. https://doi.org/10.1016/j.cherd.2017.12.011

Metzner, A.B., Otto, R.E., 1957. Agitation of non-Newtonian fluids. AIChE J. 3, 3–10. https://doi.org/10.1002/aic.690030103

Monica, M., Cushman, J.H., Cenedese, A., 2009. Application of Photogrammetric 3D-PTV Technique to Track Particles in Porous Media. Transp. Porous Med. 79, 43–65. https://doi.org/10.1007/s11242-008-9270-4

Nagata, S., Nishikawa, M., Tada, H., Gotoh, S., 1971. Power Consumption of Mixing Impellers in Pseudoplastic Liquids. J. Chem. Eng. Jpn. 4, 72–76. https://doi.org/10.1252/jcej.4.72

Norwood, K.W., Metzner, A.B., 1960. Flow patterns and mixing rates in agitated vessels. AIChE J. 6, 432–437. https://doi.org/10.1002/aic.690060317

Oliveira, J.L.G., Geld, C.W.M. van der, Kuerten, J.G.M., 2015. Lagrangian velocity and acceleration statistics of fluid and inertial particles measured in pipe flow with 3D particle tracking velocimetry. Int. J. Multiph. 73, 97–107. https://doi.org/10.1016/j.ijmultiphaseflow.2015.03.017

Ramírez-Muñoz, J., Guadarrama-Pérez, R., Márquez-Baños, V.E., 2017. A direct calculation method of the Metzner-Otto constant by using computational fluid dynamics. Chem. Eng. Sci. 174, 347–353. https://doi.org/10.1016/j.ces.2017.09.023

Rammohan, A.R., Duduković, M.P., Ranade, V.V., 2003. Eulerian Flow Field Estimation from Particle Trajectories: Numerical Experiments for Stirred Tank Type Flows. Ind. Eng. Chem. Res. 42, 2589–2601. https://doi.org/10.1021/ie020552l

Rammohan, A.R., Kemoun, A., Al-Dahhan, M.H., Dudukovic, M.P., 2001. A Lagrangian description of flows in stirred tanks via computer-automated radioactive particle tracking (CARPT). Chem. Eng. Sci. 56, 2629–2639. https://doi.org/10.1016/S0009-2509(00)00537-6

Reynolds, A.M., Mordant, N., Crawford, A.M., Bodenschatz, E., 2005. On the distribution of Lagrangian accelerations in turbulent flows. New J. Phys. 7, 58–58. https://doi.org/10.1088/1367-2630/7/1/058

Romano, M.G., Alberini, F., Liu, L., Simmons, M.J.H., Stitt, E.H., 2021. Development and application of 3D-PTV measurements to lab-scale stirred vessel flows. Chem. Eng. Res. Des. 172, 71–83. https://doi.org/10.1016/j.cherd.2021.06.001

Sánchez Pérez, J.A., Rodríguez Porcel, E.M., Casas López, J.L., Fernández Sevilla, J.M., Chisti, Y., 2006. Shear rate in stirred tank and bubble column bioreactors. Chem. Eng. J. 124, 1–5. https://doi.org/10.1016/j.cej.2006.07.002

Savitzky, A., Golay, M.J.E., 1964. Smoothing and Differentiation of Data by Simplified Least Squares Procedures. Anal. Chem. 36, 1627–1639. https://doi.org/10.1021/ac60214a047

Story, A., Jaworski, Z., Simmons, M.J., Nowak, E., 2018. Comparative PIV and LDA studies of Newtonian and non-Newtonian flows in an agitated tank. Chem. Pap. 72, 593–602. https://doi.org/10.1007/s11696-017-0307-4

Tamburini, A., Gagliano, G., Micale, G., Brucato, A., Scargiali, F., Ciofalo, M., 2018. Direct numerical simulations of creeping to early turbulent flow in unbaffled and baffled stirred tanks. Chem. Eng. Sci. 192, 161–175. https://doi.org/10.1016/j.ces.2018.07.023

Venneker, B.C.H., Derksen, J.J., Van den Akker, H.E.A., 2010. Turbulent flow of shear-thinning liquids in stirred tanks—The effects of Reynolds number and flow index. Chem. Eng. Res. Des. 88, 827–843. https://doi.org/10.1016/j.cherd.2010.01.002

Wessel, R.A., Righi, J., 1988. Generalized Correlations for Inertial Impaction of Particles on a Circular Cylinder. Aerosol Sci. Tech. 9, 29–60. https://doi.org/10.1080/02786828808959193

Willneff, J., 2003. A Spatio-Temporal Matching Algorithm for 3D Particle Tracking Velocimetry (Doctoral Thesis). Swiss Federal Institute of Technology Zurich, Zurich, Switzerland.

Zeff, B.W., Lanterman, D.D., McAllister, R., Roy, R., Kostelich, E.J., Lathrop, D.P., 2003. Measuring intense rotation and dissipation in turbulent flows. Nature 421, 146–149. https://doi.org/10.1038/nature01334

Zhou, G., Kresta, S.M., 1996. Impact of tank geometry on the maximum turbulence energy dissipation rate for impellers. AIChE J. 42, 2476–2490. https://doi.org/10.1002/aic.690420908